IEEE Access
Multidisciplinary | Rapid Review | Open Access Journal

Received July 8, 2020, accepted August 3, 2020, date of publication August 6, 2020, date of current version August 19, 2020.

Digital Object Identifier 10.1109/ACCESS.2020.3014661

A Novel Compensation Method for Eliminating Precession Angular-Rate Bias in MEMS Rate-Integrating Gyroscopes

JING LIU[1], YINGHUI YANG[1], SHUWEN GUO[1], (Member, IEEE), BO FAN[1,2], LIN XUAN[1], FENG BU[1], AND DACHENG XU[1]

[1]School of Electronic and Information Engineering, Soochow University, Suzhou 251000, China
[2]School of Electrical Engineering, South China University, Hengyang 421001, China

Corresponding author: Shuwen Guo (13862044796@163.com)

This work was supported in part by the key projects of National Natural Science Foundation of China under Grant No. 61434003.

ABSTRACT The structural asymmetry of the MEMS rate-integrating gyro (RIG) mode produces a threshold and an angle-dependent bias (ADB) that cause gyroscopes operating in this mode to stop working at input rates below the threshold and degrade the linearity of the output angle. This defect in the RIG output angle is actually caused by a precession angular-rate bias that results from both damping asymmetry (anisodamping) and stiffness asymmetry (anisostiffness). This paper describes a novel compensation method based on Fourier series fitting combined with a multiple iteration technique. The proposed compensation method can significantly reduce both the input rate threshold and ADB. Simulations indicate that the threshold and ADB caused by anisodamping and anisostiffness can be reduced by three orders of magnitude. An experimental application of this method produced a MEMS RIG threshold as low as 0.05° per second, representing an improvement of two orders of magnitude and lower than has previously been reported.

INDEX TERMS MEMS rate-integrating gyro, asymmetric damping, asymmetric stiffness, threshold.

I. INTRODUCTION

MEMS gyroscopes can operate in both rate gyro (RG) mode and rate-integration gyro (RIG) mode. RG measures the rotation rate by forcing an operational mode to oscillate steadily and detects the vibration displacement caused by the coupling of the Coriolis Effect in another mode, whereas RIG directly measures the rotation angle. In the case of RIG, the oscillation mode of the gyro maintains a consistent amplitude, and allows free precession of the oscillation pattern. The rotation angle can then be determined by measuring the precession angle of the oscillation mode.

Compared with RG, RIG has the following characteristics: (1) It can directly measure the rotation angle, which effectively reduces the accumulation error caused by angle random walk [1]; (2) RIG theoretically has unlimited bandwidth [2], [3] and input range [4]; and (3) its angular gain has extremely high stability [5]. However, the structural asymmetry of the MEMS gyroscope results in stiffness asymmetry (anisostiffness) and damping asymmetry (anisodamping) of the two oscillation modes. Anisostiffness will generate the quadrature error and frequency splitting (Δf), whereas anisodamping causes a mismatch in the gyro damping. Due to the existence of stiffness and damping anisotropy, RIG suffers from a threshold problem, that is, when the input rotation rate is below a certain value, the modal shape of the gyro will be locked at a certain angle instead of enjoying free precession, and will then not work properly in RIG mode. Moreover, anisostiffness and anisodamping are the main reasons for the angle-dependent bias (ADB) of RIG. The quadrature error [6] and frequency splitting can be reduced by quadrature electrostatic tuning and frequency electrostatic tuning [7]–[9], but they cannot be completely eliminated. Thus, the residual quadrature error and frequency splitting will still have an impact on the performance of RIG. The damping anisotropy produces a signal that is in phase with the Coriolis force, so the compensation method is somewhat complicated [10]. The method adopted in [11] generates a feedback force by analyzing the gyro dynamic equation and applying it to the gyro to cancel the impact of the damping anisotropy. However, this method assumes that the quadrature error is zero and cannot eliminate all residual errors, so only a 25% improvement can be obtained. References [12] and [13] use the virtual rotation to reduce the RIG threshold below 0.1°/s.

The associate editor coordinating the review of this manuscript and approving it for publication was Chaitanya U Kshirsagar.

This method applies a fixed force to the precession angular-rate control loop so that the oscillation pattern rotates at a constant rate, even without an input angular rate. The output angle can be obtained by subtracting the virtual rotation angle from the detected precession rotation angle. This method effectively averages the ADB and reduces the threshold. However, it cannot reduce the precession angular-rate bias. Moreover, the maximum rate of virtual rotation is limited by the hardware, which increases the difficulty of observing the rotation angle in real time. Thus, it has limited capability to improve the performance of RIG.

In summary, the above methods can reduce both the threshold and ADB to some extent, but they cannot fundamentally solve the problem of precession angular-rate bias errors introduced by the structural asymmetry of the gyro. The threshold and ADB of RIG are essentially caused by the bias terms of the anisostiffness and anisodamping in the precession angular rate of RIG [14], so the threshold and ADB could be significantly reduced by eliminating the bias terms in real time. To completely eliminate precession angular-rate bias errors, this paper introduces a novel compensation method based on a Fourier series fitting combined with a multiple iteration technique. This method uses a Fourier series to fit the precession angular-rate bias curves, and then realizes real-time compensation by adding fitting parameters to the precession angular-rate control loop of RIG.

This paper first presents a derivation of the theoretical formulas from the relevant dynamic equations, and then adds precession angular-rate bias terms associated with the damping and stiffness anisotropy. Next, a control algorithm is proposed and simulated using the Simulink software. Finally, the results of an experiment to verify the simulation results and efficiency of the proposed compensation method are presented.

II. THEORY

A. MEMS GYRO DYNAMIC EQUATION

Ideally, the MEMS gyroscope would have no asymmetry in either stiffness or damping. The ideal dynamic equation is:

$$\begin{cases} \ddot{x} + \frac{1}{\tau}\dot{x} + 2k\Omega\dot{y} + \omega^2 x = \frac{1}{M}F_x \\ \ddot{y} + \frac{1}{\tau}\dot{y} - 2k\Omega\dot{x} + \omega^2 y = \frac{1}{M}F_y \end{cases} \tag{1}$$

where x and y are the vibration signals of two orthogonal vibration modes, Ω is the input angular rate, $1/\tau$ is the damping coefficient, $\omega^2$is the stiffness coefficient, M is the effective mass of the gyro, and F_x, F_y are the feedback forces of the drive shaft and the sensitive shaft, respectively.

Under non-ideal conditions, the existences of damping and stiffness anisotropy change the gyro dynamic equation to:

$$\begin{bmatrix} \ddot{x} \\ \ddot{y} \end{bmatrix} + \begin{bmatrix} \left(\frac{2}{\tau}\right) + \left(\Delta\frac{1}{\tau}\right)\cos 2\theta_\tau & \left(\Delta\frac{1}{\tau}\right)\sin 2\theta_\tau \\ \left(\Delta\frac{1}{\tau}\right)\sin 2\theta_\tau & \left(\frac{2}{\tau}\right) - \left(\Delta\frac{1}{\tau}\right)\cos 2\theta_\tau \end{bmatrix} \begin{bmatrix} \dot{x} \\ \dot{y} \end{bmatrix} + \begin{bmatrix} 0 & -2k\Omega \\ 2k\Omega & 0 \end{bmatrix} \begin{bmatrix} \dot{x} \\ \dot{y} \end{bmatrix} + \begin{bmatrix} \omega^2 + \omega\Delta\omega\cos 2\theta_\omega & \omega\Delta\omega\sin 2\theta_\omega \\ \omega\Delta\omega\sin 2\theta_\omega & \omega^2 - \omega\Delta\omega\cos 2\theta_\omega \end{bmatrix} \begin{bmatrix} x \\ y \end{bmatrix} = \frac{1}{M}\begin{bmatrix} f_x \\ f_y \end{bmatrix} \tag{2}$$

where $\omega\Delta\omega = \frac{\omega_x^2 - \omega_y^2}{2}$, ω_x, ω_y are the x-modal and y-modal resonance frequencies, respectively, k is the angular gain, θ_τ, θ_ω are the included angles between the damping principal axis and stiffness principal axis, respectively, and $\Delta(1/\tau)$ is the damping error.

Ideally, the vibration pattern of RIG is a straight line. However, in the non-ideal situation, the quadrature force caused by the structure error produces an elliptical RIG vibration pattern, as shown in Fig. 1.

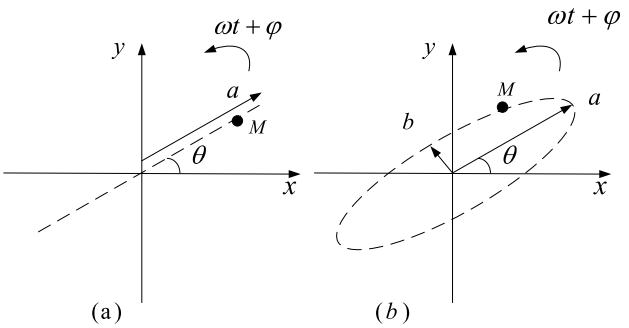

FIGURE 1. Illustration of ideal and non-ideal vibration patterns of RIG. (a) In the ideal RIG, the vibration pattern moves on a single axis with amplitude a. (b) In the non-ideal RIG, quadrature error causes the vibration pattern to become an ellipse.

B. CONTROL ALGORITHM

From Fig. 1(b), we can derive the x-modal and y-modal motion equations as:

$$\begin{cases} x = a\cos\theta\cos(\omega t + \varphi) - b\sin\theta\sin(\omega t + \varphi) \\ y = a\sin\theta\cos(\omega t + \varphi) + b\cos\theta\sin(\omega t + \varphi) \end{cases} \tag{3}$$

As the vibration energy of RIG will be attenuated, it is necessary to control the vibration energy so that it remains constant. In addition, to reduce the impact of the quadrature force on the performance of the gyro, it is necessary to control the quadrature signal to make it as small as possible. To obtain the vibration energy signal and the quadrature signal, the detection signal can be demodulated by multiplication to obtain the following four vibration pattern parameters:

$$\begin{cases} x_c = a\cos\theta\cos\varphi + b\sin\theta\sin\varphi \\ x_s = a\cos\theta\sin\varphi - b\sin\theta\cos\varphi \\ y_c = a\sin\theta\cos\varphi - b\cos\theta\sin\varphi \\ y_s = a\cos\theta\sin\varphi + b\cos\theta\cos\varphi \end{cases} \tag{4}$$

The required control parameters are then obtained by combining these four mode parameters as follows:

$$\begin{cases} E = a^2 + b^2 = x_c^2 + x_s^2 + y_c^2 + y_s^2 \\ Q = 2ab = 2(x_c y_s - x_s y_c) \\ R = \left(a^2 - b^2\right)\cos 2\theta = x_c^2 + x_s^2 - y_c^2 - y_s^2 \\ S = \left(a^2 - \mathrm{b}^2\right)\sin 2\theta = 2\left(x_c y_c + x_s y_s\right) \\ \theta = \dfrac{1}{2}\arctan\left(\dfrac{S}{R}\right) \\ \varphi = 0.5\arctan\dfrac{2\left(x_c x_s + y_c y_s\right)}{x_c^2 - x_s^2 + y_c^2 - y_s^2} \end{cases} \tag{5}$$

where E is the energy variable, Q is the quadrature variable, S and R are used to determine the precession angle θ, and φ is used to track the frequency of the resonator. As the output range of the arctan function is $[-\pi, \pi]$, the range of θ is $[-\pi/2, \pi/2]$, which does not cover the full $[-\pi, \pi]$ range of θ. Thus, a revised angle function with an extended angle range is used in our control method:

$$\theta = \frac{1}{2}\arctan\left(\frac{S}{R}\right) + \begin{cases} \pi, & x_c < 0 \& S < 0 \\ 0, & x_c > 0 \\ -\pi, & x_c < 0 \& S > 0 \end{cases} \tag{6}$$

The RIG control system generally has three control loops: energy control loop, quadrature control loop, and precession angular-rate control loop. The energy control loop and the quadrature control loop use a proportional-integral (PI) feedback controller [15]–[17] to maintain the vibration amplitude and minimize the quadrature error. The precession angular-rate control loop can superimpose a variable virtual rate on the precession angular rate to compensate the precession angular-rate bias error. Equations (7)–(9) are the expressions used for the input force of the energy control loop, quadrature control loop, and precession angular-rate control loop.

$$F_E = K_{PE}\left(E_0 - E\right) + K_{IE}\int_0^\tau \left(E_0 - E\left(\tau\right)\right)d\tau \tag{7}$$

where F_E is the vibration energy PI controller output, K_{PE} and K_{IE} are PI parameters, and E_0 is the vibration energy reference value.

$$F_Q = -K_{PQ}Q - K_{IQ}\int_0^\tau Q\left(\tau\right)d\tau \tag{8}$$

where F_{Q} is the vibration energy PI controller output.

$$\dot{\theta} = -k\Omega + \frac{1}{2}\Delta\left(\frac{1}{\tau}\right)\sin\ 2\left(\theta - \theta_\tau\right) + \frac{1}{2}\Delta\omega\cos 2\left(\theta - \theta_\omega\right)\frac{Q}{E} - \frac{F_{\dot{\theta}}}{2\omega\sqrt{E}} \tag{9}$$

where $\dot{\theta}$ is the precession angular rate and $F_{\dot{\theta}}$ is the angle-dependent control force that is applied to the precession angular-rate control loop. The precession angular-rate bias terms caused by anisodamping and anisostiffness are described in (9). It can be seen that the bias terms result in some problems, such as a threshold and ADB.

Through these three control loops, the feedback forces $F_{\mathbf{x}}$ and F_y in the x and y modes can be generated using:

$$\begin{cases} F_x = F_E\cos\theta\sin\omega t - F_Q\sin\theta\cos\omega t - F_{\dot{\theta}}\sin\theta\sin\omega t \\ F_y = F_E\sin\theta\sin\omega t + F_Q\cos\theta\cos\omega t + F_{\dot{\theta}}\cos\theta\sin\omega t \end{cases} \tag{10}$$

This equation is used to compensate for the anisodamping and anisostiffness effects. The compensation process is discussed in the following subsections.

C. COMPENSATION FOR DAMPING ERROR

When only anisodamping is present, the RIG precession angular rate can be expressed as:

$$\dot{\theta} = -k\Omega + \frac{1}{2}\Delta\left(\frac{1}{\tau}\right)\sin 2\left(\theta - \theta_\tau\right) \tag{11}$$

For $\Omega < \frac{1}{2k}\Delta\left(\frac{1}{\tau}\right)$, as the precession angle θ changes, $\dot{\theta}$ will eventually become 0, and the precession angle of the resonator mode will be fixed at an angle of $\theta_{lock}(\theta_{lock} \approx \theta_\tau + \frac{1}{2}\arcsin\left(\frac{2k\Omega}{\Delta\left(\frac{1}{\tau}\right)}\right)$.

To compensate the precession angular-rate bias caused by damping anisotropy, the force $F_{\Delta\frac{1}{\tau}}$ is applied to the precession angular-rate control loop as:

$$\dot{\theta} = -k\Omega + \frac{1}{2}\Delta\left(\frac{1}{\tau}\right)\sin 2\left(\theta - \theta_\tau\right) - \frac{F_{\Delta\frac{1}{\tau}}}{2\omega\sqrt{E}} \tag{12}$$

By setting$F_{\Delta\frac{1}{\tau}}(\theta) = \omega\sqrt{E}\Delta\left(\frac{1}{\tau}\right)\sin\ 2\left(\theta - \theta_\tau\right)$, the damping error term is compensated in real time. Fig. 2(a) shows simulation data for the angular-rate bias caused by anisodamping when the input angular rate without compensation is 100°/s. This value is about ±7.5°/s, which means that the RIG threshold is 7.5°/s. After compensating for the damping error term in the precession angular rate, we can see from Figs. 2(c) and 2(d) that the precession angular-rate bias and ADB have been reduced by three orders of magnitude. The relevant simulation parameters are presented in Table 1.

D. COMPENSATION FOR STIFFNESS ERROR

When only anisostiffness is present, the RIG precession angular rate can be expressed as:

$$\dot{\theta} = -k\Omega + \frac{1}{2}\Delta\omega\cos 2\left(\theta - \theta_\omega\right)\frac{Q}{E} \tag{13}$$

As the quadrature signal Q is also a function of θ, the impact of anisostiffness on the precession angular rate is not only a fluctuation of 2θ, but also the $n\theta$ harmonics, which increase the difficulty of anisostiffness compensation. Therefore, to reduce the stiffness error term, a more complex force $F_{\Delta\omega}$ needs to be added to the precession angular-rate

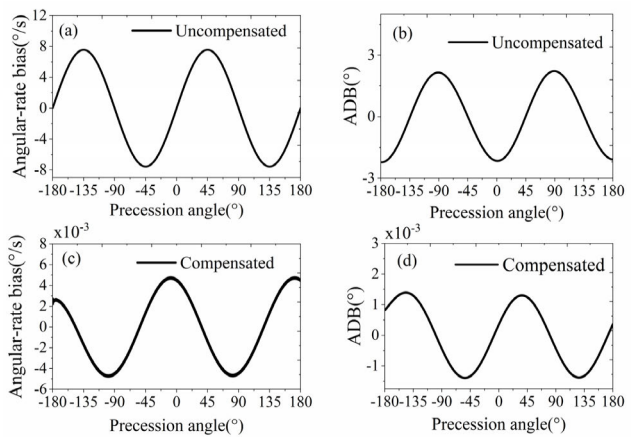

FIGURE 2. Simulation diagram of ADB and angular-rate bias before and after compensation of damping error terms. (a) Precession angular-rate bias without compensation. (b) ADB without compensation. (c) Precession angular-rate bias after compensation has improved by three orders of magnitude compared with before. (d) ADB after compensation has also improved by three orders of magnitude compared with before.

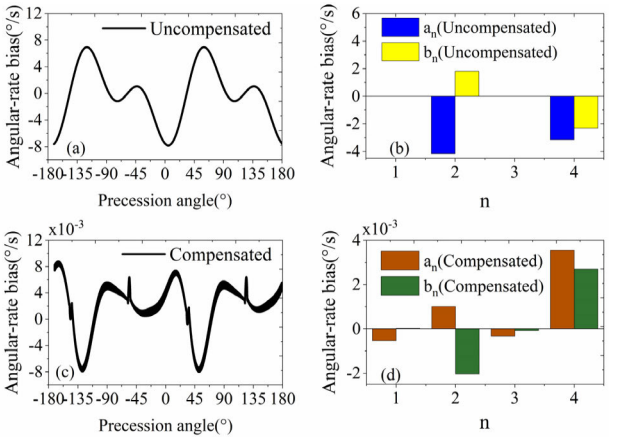

FIGURE 3. Fitting function parameter diagram of angular-rate bias before and after compensation of stiffness error terms. (a) Precession angular-rate bias without compensation. (b) Fitting parameters of precession angular-rate bias without compensation. (c) Precession angular-rate bias after compensation. (d) Fitting parameters of precession angular-rate bias after compensation.

TABLE 1. Simulation parameters related to anisodamping compensation.

Parameter	Value	Units
f_c	5045	Hz
k	1	\
Ω	100	°/s
Δf	0	Hz
$\Delta(1/\tau)$	0.2643	rad
$\sqrt{E}$	0.2	μm
θ_τ	0	°

TABLE 2. Simulation parameters related to an ISO stiffness compensation.

Parameter	Value	Units
f_c	5045	Hz
k	1	\
Ω	100	°/s
Δf	1	Hz
$\Delta(1/\tau)$	0	rad
$\sqrt{E}$	0.2	μm
θ_ω	30	°

control loop. This is formed by superimposing multiple signals. Although this force is very complex, we can use the Fourier series harmonics information in (14). The accurate compensation parameters will then be generated by fitting the measured precession angular-rate bias curve using (14).

$$\frac{F_{\Delta\omega}(\theta)}{2\omega\sqrt{E}} = \sum_{n=1}^{\infty}(a_n \cos n\theta + b_n \sin n\theta) \tag{14}$$

Fig. 3 is a simulation diagram of the precession angular-rate bias before and after compensation for anisostiffness. The relevant simulation parameters are presented in Table 2. Fig. 3(a) illustrates that the error term for the anisostiffness with respect to the precession angular rate contains harmonics, and that the threshold is about 8°/s. Reference [10] shows that the harmonics of 2θ and 4θ occupy the dominant part of the RIG error, so we set $n = 4$ in (14) and then perform data fitting. The results using the fitting parameters obtained in this way are shown in Fig. 3(b). The precession angular-rate error after compensation, as illustrated in Fig. 3(c), has been improved by three orders of magnitude. Although the compensation method can effectively reduce the impact of anisostiffness, the presence of harmonics makes the compensation scheme complicated. Hence, the harmonics of the error should first be reduced by using quadrature electrostatic tuning to decrease the quadrature error, as this makes the compensation scheme simpler.

In addition, compensation for the anisostiffness can be extended to cases where anisodamping and anisostiffness exist at the same time. For this purpose, the input force $F_{\dot{\theta}}$ of the precession angular-rate control loop can be included in (14). Therefore, the damping and stiffness error terms can be compensated simultaneously using the expression:

$$\frac{F_{\dot{\theta}}}{2\omega\sqrt{E}} = \frac{F_{\Delta\frac{1}{\tau}} + F_{\Delta\omega}}{2\omega\sqrt{E}} = \sum_{n=1}^{\infty}(\alpha_n \cos n\theta + \beta_n \sin n\theta) \tag{15}$$

III. EXPERIMENTS AND ANALYSIS

A. TEST PLATFORM AND GYRO PARAMETERS

A fully vacuum-encapsulated cobweb-like disk resonator gyroscope (DRG) [15] was used in the experiments. Fig. 4 shows a structural diagram and vibration mode diagram of the cobweb-like DRG, in which vibration in the 0°

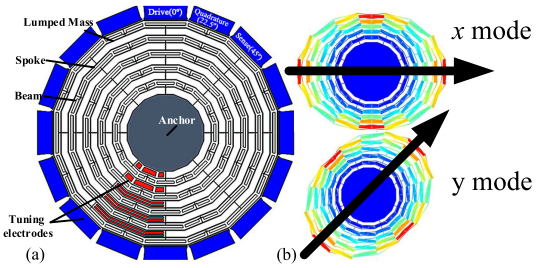

FIGURE 4. Cobweb-like DRG structure diagram and mode shapes diagram. (a) The structure is polygonal and highly symmetric. (B) n =2 mode shapes diagram [8], where the 0° direction is the x mode and 45° direction is the y mode.

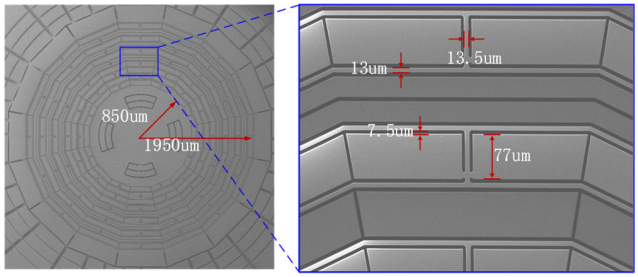

FIGURE 5. SEM overview and magnified view of photos of a fabricated cobweb-like DRG.

direction is the x mode and vibration in the 45° direction is the y mode. The cobweb-like DRG is composed of 10 concentric polygonal spider web rings connected by eight spokes to a single central anchor. Each ring is connected by 16 identical rectangular beams. The diameter of the outermost ring is 3.8 mm, the diameter of the central anchor is 1.7 mm, the width of the polygonal ring is 13 μm, and the width of the lumped mass on the ring is 77 μm. As the cobweb-like DRG has an extremely highly symmetric structure, its damping asymmetry and stiffness asymmetry are much smaller than in conventional DRGs [18]. Table 3 presents some parameters of the cobweb-like DRG.

TABLE 3. Main parameters of the cobweb-like DRG.

Parameter	Value	Units
f_c	5045.93	Hz
Δf	1.66	Hz
Q_x	136252	\
Q_y	135606	\
$\Delta(1/\tau)$	5.35×10^{-4}	rad
k	0.77	\
M	4.5×10^{-7}	kg

After electrostatic tuning of the quadrature error, the resonance frequency of the cobweb-like DRG was tested at room temperature. First, a sweeping frequency AC signal with a frequency of 5044–5048 Hz and a sweep interval of 0.01 Hz was produced by a signal generator (KEYSIGHT 33500B)

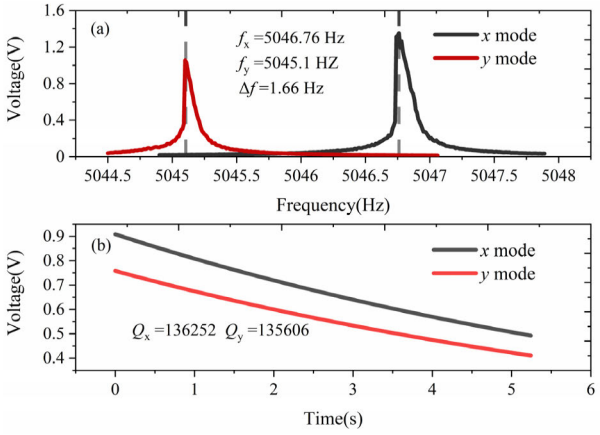

FIGURE 6. Frequency sweep and attenuation of two modes. (a) Frequency sweep curves obtained by sweeping the two modes of the gyro at intervals of 0.01 Hz. (b) Energy decay curves of the two modes. The measured quality factor values of the x mode and y mode are 136252 and 135606, respectively.

to drive the gyroscope. An NI acquisition card collected the vibration signals of the two modes of the gyro, and the resulting curves are shown in Fig. 6(a). The frequency split between the two modes of the gyroscope is 1.66 Hz with only the electrostatic tuning of the quadrature error.

The quality factor was measured using a time decay method. After the vibration of the gyroscope had stabilized, the drive signal was turned off so that the vibration energy of the gyroscope could freely attenuate. The resulting attenuation curve is shown in Fig. 6(b). The measured quality factors of the x and y modes are 136252 and 135606, respectively. Thus, we can calculate $\Delta(1/\tau) = 5.35 \times 10^{-4}$ rad. and the corresponding threshold value is 0.02°/s. This means that the cobweb-like DRG has very high structural symmetry.

Fig. 7 shows the RIG test platform. The gyro is soldered onto a PCB, and the input angular rate is provided by a rate table. The output signal is then extracted by the read-out circuit on the printed circuit board (PCB). The analog-to-digital converters (ADC) uses the 18-bit serial output ADS8881 with a sampling rate of 625 kHz. The digital-to-analog converters (DAC) uses a 16-bit high-accuracy DAC8831. The RIG control system was built using a Field Programmable Gate Array (FPGA), and the signals were collected through the serial port using a LabVIEW program with a sample rate of 90 Hz. Fig. 8 shows a block diagram of the RIG control system.

B. PRECESSION ANGULAR-RATE BIAS

The threshold and ADB are the two most important performance indicators of RIG. The former causes RIG to fail when the input angular rate is below the threshold, and the latter degrades the linearity of the angle output at low speeds. Therefore, RIG is often suitable for high input angular rates.

In theory, the angular gain of the cobweb-like DRG is 0.77 [8]. To verify the stability of the RIG angular gain, the output angle was measured in clockwise

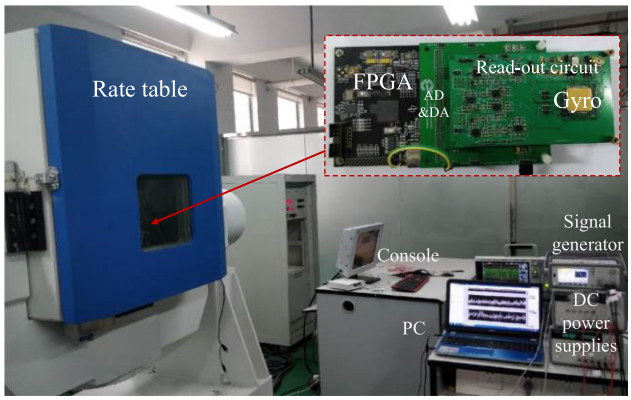

FIGURE 7. RIG control circuit. The control circuit is divided into three parts. The first part is the gyro interface circuit, which is used to extract gyro signals. The gyro is welded onto the interface circuit board. The second part includes the ADC and DAC, which are used for the conversion of digital and analog signals. The third part is the FGPA, which is used to realize the RIG control program.

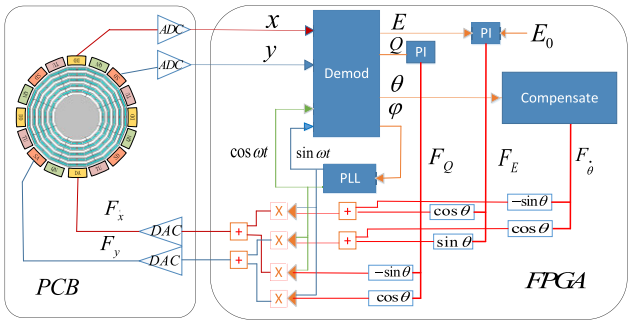

FIGURE 8. Block diagram of RIG control system. The Demod module in the FPGA is used to demodulate the required control signals, the PLL module is used to track the resonance frequency of the gyro, and the Compensate module is used to compensate the precession angular-rate bias.

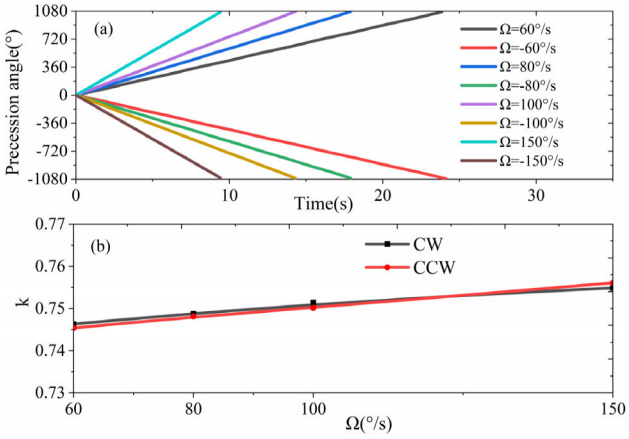

FIGURE 9. Output angle and angular gain of RIG at different speeds. (a) Output angle of RIG as the rate table speed changed from 60–150°/s. (b) Angular gain becomes closer to the theoretical value as the speed increases.

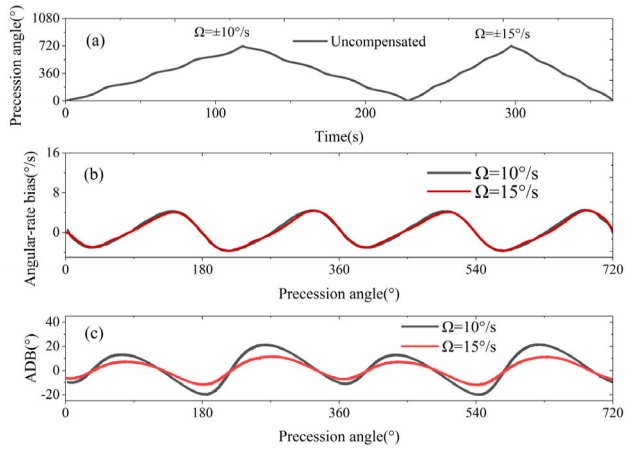

FIGURE 10. RIG output angle and related errors when the input angular rate is ±10–15°/s before compensation. (a) Output angle when the input angular rate is 10–15°/s. (b) Precession angular-rate bias when the input angular rate is 10–15°/s. As the input angular rate changes, the precession angular-rate bias will not change. In this case, the threshold is 5°/s. (c) ADB decreases gradually as the input angular rate increases.

and counterclockwise directions with an input angular rate of 60–150°/s (Fig. 9(a)). Once the precession angle had rotated for three cycles, its angular gain k was calculated. As the input angular rate Ω increases, we see from Fig. 9(b) that the angular gain k tends to 0.77, which is consistent with the characteristics of RIG [20].

For RIG, as the input angular rate increases, ADB will gradually decrease, and the output angle linearity will improve. This is because a higher speed entails a greater degree of averaging of ADB. However, the RIG precession angular-rate bias caused by stiffness and damping anisotropy will not decrease as the input angular rate increases. Thus, even when the input angular rate is high, the precession angular-rate bias will still exist. This significantly affects the linearity of the RIG output angle at low speeds. Therefore, it is important to compensate the precession angular-rate bias in order to reduce the threshold and ADB.

Fig. 10 illustrates the output angle and related errors of RIG when the input angular rate is ±10–15°/s without compensation. From the output of RIG, the effects of anisostiffness and anisodamping are reflected in the bias of the output angle, and this angular bias decreases as the input angular rate increases (Figs. 10(a), 10(c)). In essence, however, the RIG precession angular rate will drift under non-ideal conditions (Fig. 10(b)). The maximum drift value is the threshold of RIG. This bias will not change with the input angular rate, and will produce $n\theta$ harmonics due to the existence of anisostiffness.

In addition, the RIG precession angular-rate bias information can be derived from the output angle and then smoothed using a MATLAB tool.

C. PRECESSION ANGULAR-RATE BIAS COMPENSATION

After obtaining the precession angular-rate bias curve, (15) can be used to fit the error curve and generate the relevant fitting parameters. These fitting parameters are used in the precession rate control loop to perform bias compensation. As shown in Fig. 11(a), the bias of the RIG output

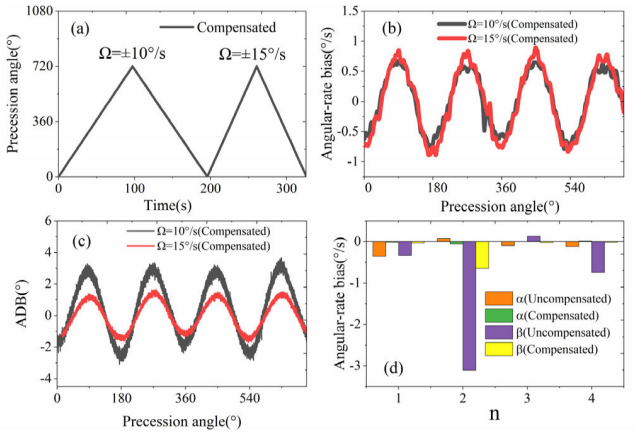

FIGURE 11. Output angle and related errors of RIG when the input angular rate is 10–15°/s after compensation. (a) Output angle when the input angular rate is ±10–15°/s after compensation. (b) Precession angular-rate bias when the input angular rate is 10–15°/s. (c) ADB when the input angular rate is 10–15°/s; the precession angular-rate bias and ADB have improved by a factor of five after compensation. (d) Fitting parameters of precession angular-rate bias before and after compensation.

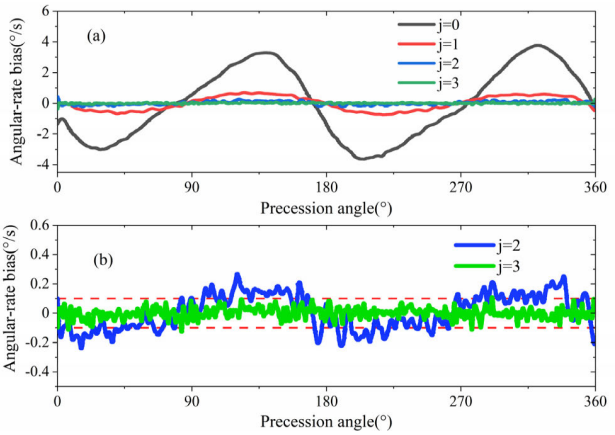

FIGURE 12. Precession angular-rate bias after j iterations of compensation. (a) Precession angular-rate bias after j =0, 1, 2, and 3 iterations. (b) Precession angular-rate bias when j =2 and j =3. By the third iteration, the precession angular-rate bias is less than 0.1°/s.

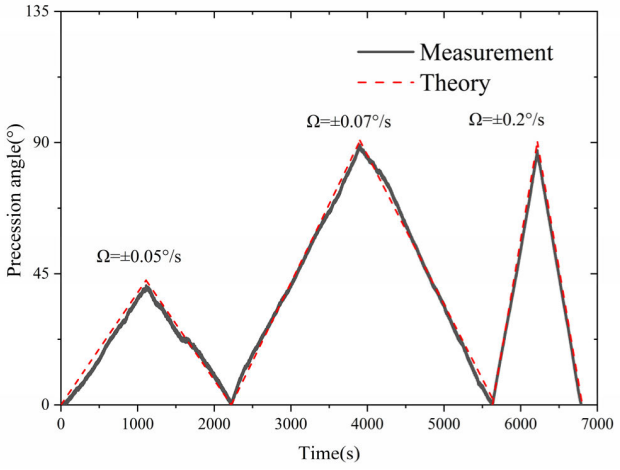

FIGURE 13. Output angle when the input angular rate is ±0.05–0.2°/s. After three iterations of compensation, the threshold is less than 0.05°/s.

angle is improved after compensation, and the precession angular-rate bias and ADB have been reduced by a factor of five (Figs. 11(b), 11(c)). Fig. 11(d) illustrates the effect of the fitting parameters obtained by fitting the precession angular-rate bias before and after compensation. It can be seen that only the 2θ harmonic is dominant in the precession angular-rate bias after compensation.

Although the precession angular-rate bias improved after compensation, the remaining harmonic error still produces a 1°/s threshold. To further reduce this value, the remaining precession angular-rate bias can be fitted and compensated again. This iterative improvement is another advantage of the precession angular-rate bias compensation method.

By iteratively calculating the remaining error, the final precession angular-rate bias will be reduced to a level below the circuit noise. Equation (15) can be improved as follows:

$$\frac{F_{\dot{\theta}}}{2\omega\sqrt{E}} = \sum_{j=0}^{\infty}\left(\sum_{n=1}^{\infty}\left(\alpha_{jn}\cos n\theta + \beta_{jn}\sin n\theta\right)\right) \qquad (16)$$

where j represents the number of iterations and $j = 0$ represents the precession angular-rate bias before compensation. In theory, as long as the noise of the control system is sufficiently low, the threshold of the gyro after an infinite number of iterations will eventually be close to 0°/s. In practice, as the circuit noise [21] will submerge the signal of the precession angular-rate bias, the circuit noise must be reduced to further improve the RIG performance.

It can be seen from Fig. 12(a) that the first compensation reduces the threshold from 5°/s to 1°/s. After the second iteration of compensation, the threshold is further reduced to 0.2°/s (Fig. 12(b)). In the third and final iteration of the compensation process, the threshold decreases to below 0.1°/s. The precession angular-rate bias information was then completely submerged by circuit noise, so it is difficult to continue the iterative process. Fig. 13 shows the output angle for input angular rates from ±0.05–0.2°/s. The threshold finally decreases to below 0.05°/s. This represents an improvement by two orders of magnitude after compensation; the threshold could be further reduced after lowering the circuit noise.

Experiments show that the proposed compensation method based on a Fourier series fitting technique, after multiple iterations, can efficiently reduce the RIG threshold. After three iterations of compensation, the threshold has been reduced by two orders of magnitude. Fig. 14 shows the precession angular rate obtained by differentiating and smoothing the output angle for input angular rates of ±0.05–0.2°/s. The precession angular rate should be equal to the input angular rate Ω multiplied by the angular gain k (=0.77). The resolution drops to 0.05°/s or less after compensation; the exact value is limited by the circuit noise.

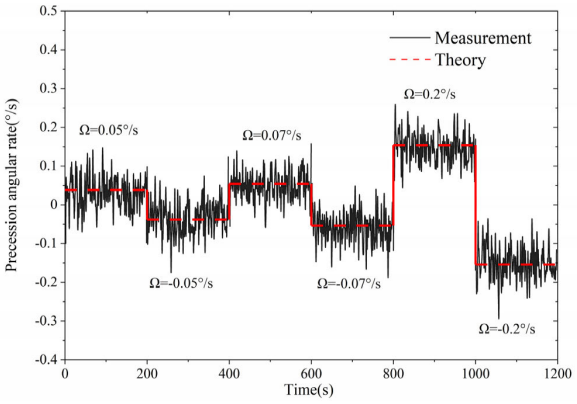

FIGURE 14. Precession angular rates at input angular rates of ±0.05–0.2°/s rotation.

D. DISCUSSION

In general, the RIG output angle should be derived and smoothed before compensation to determine the bias curves. The compensation parameters can then be generated by fitting the measured precession angular-rate bias curves using a Fourier series and multiple iterations. Finally, a fitting compensation force is applied to the precession angular-rate control loop. We have demonstrated that this method significantly reduces the precession angular-rate bias. The advantages of this method are that the bias errors caused by both anisodamping and anisostiffness can be compensated simultaneously. In theory, the error can be completely eliminated by increasing the number of iterations, but the circuit noise imposes a limitation on this method. Therefore, it is necessary to minimize the circuit noise to achieve a lower threshold.

IV. CONCLUSION

In this paper, we have proposed a novel method for precession angular-rate bias error compensation in an attempt to reduce the threshold and ADB of RIG. The threshold of a MEMS cobweb-like DRG was successfully reduced to less than 0.05°/s, which is the lowest threshold for MEMS RIG. However, the precession angular-rate bias signal becomes submerged by the circuit noise at this point, and so the threshold can only be further reduced if the circuit noise is decreased.

The proposed method provides a highly efficient means of improving the threshold and ADB of RIG, offering a breakthrough in achieving high-precision MEMS RIG. Moreover, our method can be applied to other axially symmetric RIG structures, such as hemispherical gyros.

REFERENCES

[1] C. C. Painter and A. M. Shkel, "Structural and thermal modeling of a z-axis rate integrating gyroscope," *J. Micromech. Microeng.*, vol. 13, no. 2, p. 229, 2003.

[2] A. A. Trusov, I. P. Prikhodko, S. A. Zotov, A. R. Schofield, and A. M. Shkel, "Ultra-high q silicon gyroscopes with interchangeable rate and whole angle modes of operation," in *Proc. IEEE Sensors*, Kona, HI, USA, Nov. 2010, pp. 864–867, doi: 10.1109/ICSENS.2010.5690867.

[3] C. C. Painter and A. M. Shkel, "Active structural error suppression in MEMS vibratory rate integrating gyroscopes," *IEEE Sensors J.*, vol. 3, no. 5, pp. 595–606, Oct. 2003.

[4] N. Yazdi, F. Ayazi, and K. Najafi, "Micromachined inertial sensors," *Proc. IEEE*, vol. 86, no. 8, pp. 1640–1659, Aug. 1998.

[5] J. Cho, J. A. Gregory, and K. Najafi, "High-Q, 3 kHz Single-Crystal-Silicon cylindrical rate-integrating gyro (CING)," in *Proc. IEEE 25th Int. Conf. Micro Electro Mech. Syst. (MEMS)*, Paris, France, Jan. 2012, pp. 172–175.

[6] F. Bu, S. Guo, M. Cheng, F. Zheng, D. Xu, and H. Zhao, "Effect of circuit phase delay on bias stability of MEMS gyroscope under force rebalance detection and self-compensation method," *J. Micromech. Microeng.*, vol. 29, no. 9, Sep. 2019, Art. no. 095002.

[7] B. J. Gallacher, J. Hedley, J. S. Burdess, A. J. Harris, A. Rickard, and D. O. King, "Electrostatic correction of structural imperfections present in a microring gyroscope," *J. Microelectromech. Syst.*, vol. 14, no. 2, pp. 221–234, Apr. 2005.

[8] T.-H. Su, S. H. Nitzan, P. Taheri-Tehrani, M. H. Kline, B. E. Boser, and D. A. Horsley, "Silicon MEMS disk resonator gyroscope with an integrated CMOS analog front-end," *IEEE Sensors J.*, vol. 14, no. 10, pp. 3426–3432, Oct. 2014.

[9] F. Bu, D. Xu, H. Zhao, B. Fan, and M. Cheng, "MEMS gyroscope automatic real-time mode-matching method based on phase-shifted 45° additional force demodulation," *Sensors*, vol. 18, no. 9, p. 3001, Sep. 2018.

[10] P. Taheri-Tehrani, A. D. Challoner, and D. A. Horsley, "Micromechanical rate integrating gyroscope with angle-dependent bias compensation using a self-precession method," *IEEE Sensors J.*, vol. 18, no. 9, pp. 3533–3543, May 2018.

[11] J. A. Gregory, J. Cho, and K. Najafi, "Novel mismatch compensation methods for rate-integrating gyroscopes," in *Proc. IEEE/ION Position, Location Navigat. Symp.*, Myrtle Beach, SC, USA, Apr. 2012, pp. 252–258.

[12] I. P. Prikhodko, J. A. Gregory, D. I. Bugrov, and M. W. Judy, "Overcoming limitations of rate integrating gyroscopes by virtual rotation," in *Proc. IEEE Int. Symp. Inertial Sensors Syst.*, Laguna Beach, CA, USA, Feb. 2016, pp. 5–8.

[13] I. P. Prikhodko, J. A. Gregory, and M. W. Judy, "Virtually rotated MEMS gyroscope with angle output," in *Proc. IEEE 30th Int. Conf. Micro Electro Mech. Syst. (MEMS)*, Las Vegas, NV, USA, Jan. 2017, pp. 323–326.

[14] P. Taheri-Tehrani, O. Izyumin, I. Izyumin, C. H. Ahn, E. J. Ng, V. A. Hong, Y. Yang, T. W. Kenny, B. E. Boser, and D. A. Horsley, "Disk resonator gyroscope with whole-angle mode operation," in *Proc. IEEE Int. Symp. Inertial Sensors Syst. (ISISS)*, Hapuna Beach, HI, USA, Mar. 2015, pp. 1–4.

[15] C. He, Q. Zhao, Y. Liu, Z. Yang, and G. Yan, "Closed loop control design for the sense mode of micromachined vibratory gyroscopes," *Sci. China Technol. Sci.*, vol. 56, no. 5, pp. 1112–1118, May 2013.

[16] C. He, Q. Zhao, Q. Huang, L. Lin, Z. Yang, D. Zhang, and G. Yan, "A novel robust design method for the sense mode of a MEMS vibratory gyroscope based on fuzzy reliability and taguchi design," *Sci. China Technol. Sci.*, vol. 60, no. 2, pp. 317–324, Feb. 2017.

[17] R. Guan, C. He, D. Liu, Q. Zhao, Z. Yang, and G. Yan, "A temperature control system used for improving resonant frequency drift of MEMS gyroscopes," in *Proc. 10th IEEE Int. Conf. Nano/Micro Engineered Mol. Syst.*, Apr. 2015, pp. 397–400.

[18] B. Fan, S. Guo, M. Cheng, L. Yu, M. Zhou, W. Hu, F. Zheng, F. Bu, and D. Xu, "Frequency symmetry comparison of cobweb-like disk resonator gyroscope with ring-like disk resonator gyroscope," *IEEE Electron Device Lett.*, vol. 40, no. 9, pp. 1515–1518, Sep. 2019.

[19] B. Fan, S. Guo, L. Yu, M. Cheng, M. Zhou, W. Hu, F. Zheng, and D. Xu, "A novel sixteen-sided cobweb-like disk resonator gyroscope with low as-fabricated frequency split between drive and sense modes," in *Proc. IEEE SENSORS*, New Delhi, India, Oct. 2018, pp. 578–581.

[20] M. Song, B. Zhou, T. Zhang, B. Hou, and R. Zhang, "Parametric drive of a micro rate integrating gyroscope using discrete electrodes," in *Proc. IEEE Int. Symp. Inertial Sensors Syst. (INERTIAL)*, Kauai, HI, USA, Mar. 2017, pp. 70–73.

[21] F. Bu, X. Wang, B. Fan, S. Guo, D. Xu, X. Xu, and H. Zhao, "Noise model considering electrical feed-through under force rebalance closed-loop detection of MEMS gyroscope," *J. Micromech. Microeng.*, vol. 30, no. 5, May 2020, Art. no. 055007.

JING LIU is currently pursuing the M.S. degree in electronic and communication engineering with the School of Electronic and Information Engineering, Soochow University, Suzhou, China. His current research interests include control and signal processing technology of MEMS sensors.

YINGHUI YANG is currently pursuing the M.S. degree in integrated circuit with the School of Electronic and Information Engineering, Soochow University, Suzhou, China. Her current research interests include control and signal processing technology of MEMS sensors.

SHUWEN GUO (Member, IEEE) received the Ph.D. degree in semiconductor device physics from the Laboratories of Transducer Technology, Shanghai Institute of Metallurgy, Academia Sinica, China, in 1990.

He was a Visiting Scientist in applied physics with the Department of Physics and Measurement Technology, Linköping University, Sweden, from 1993 to 1995. He was a Research and Development Engineer with the Micro-Systems Group, Inter-University Micro-Electronics Center (IMEC), Belgium, from 1995 to 1996. He continued his research with Case Western Reserve University, as a Senior Principal Researcher, from 1996 to 1999. He was also a Senior Principal Engineer (Research and Development) with the Aircraft Sensors Division, Goodrich Corporation (United Technologies, since 2012), from 2000 to 2012. He joined Soochow University (PRC), in 2012, where he is currently a Professor with the Electronic Information College. He has authored or coauthored more than 50 papers in refereed journals and conference proceedings. He holds over 21 U.S. patents and more than ten Chinese patents in MEMS gyroscope, accelerometer, and pressure sensors. His research interests include design, modeling, and fabrication of MEMS sensors.

BO FAN received the B.S., M.S., and Ph.D. degrees from the School of Electronic and Information Engineering, Soochow University, Soochow, China, in 2013, 2016, and 2020, respectively. He is currently a Faculty Member with the Institute of Communication Engineering, South China University. His research interests include structure design and analysis of microsystem modeling for micro-electro-mechanical systems (MEMS) inertial sensors.

LIN XUAN is currently pursuing the M.S. degree in electronic science and technology with the School of Electronic and Information Engineering, Soochow University, Suzhou, China. Her current research interests include structure design and signal processing technology of MEMS sensors.

FENG BU received the M.S. degree in electronic and communication engineering from Shanghai Normal University, Shanghai, China, in 2014, and the Ph.D. degree in signal and information processing from Soochow University, Suzhou, China, in 2020. His research interests include measurement, control, and signal processing technology of MEMS inertial sensors.

DACHENG XU received the B.S. degree in physics education from Northwest Normal University, Gansu, China, in 1984, and the M.S. degree in circuits and systems from the University of Electronic Science and Technology, Sichuan, China, in 1992.

He was a Visiting Scholar with the University of Twente, Enschede, The Netherlands, and the National University of Singapore, Singapore. He is currently a Professor with the Department of Electronics and Information, Soochow University, Suzhou, China. His research interests include vibration energy harvester signal processing, MEMS inertial sensor circuit designing, and measurement technology.